Journal of Manufacturing Processes 168 (2026) 508–523

Contents lists available at ScienceDirect

Journal of Manufacturing Processes

journal homepage: www.elsevier.com/locate/manpro

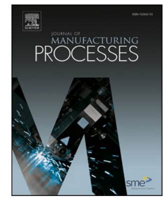

Ultrasonic vibration-assisted scratching of A-plane sapphire: Atomistic damage mechanisms and a damage-activation model

Yuqiang Zhang [a,b,c], Zhongwei Hu [a,b,*], Yiqing Yu [b], Xipeng Xu [a,b,**], Wenhan Zeng [c,***], Wenbin Zhong [c], Qing Peng [d], Liam Blunt [c], Xiangqian Jiang [c]

[a] Institute of Manufacturing Engineering, Huaqiao University, Xiamen, China
[b] State Key Laboratory for High Performance Tools, Huaqiao University, Xiamen, China
[c] EPSRC Future Metrology Hub, Centre for Precision Technologies, School of Computing and Engineering, University of Huddersfield, UK
[d] Hubei Key Laboratory of Electronic Manufacturing and Packaging Integration, Wuhan University, Wuhan, China

HIGHLIGHTS

- Elucidates how vibration parameters and crystal orientation affect subsurface damage on the A-plane
- Reveals the competition between dislocation slip and deformation twinning under UVAS
- Proposes an ultrasonically modulated damage-activation model
- Provides a predictive framework for optimizing UVAS of anisotropic sapphire

GRAPHICAL ABSTRACT

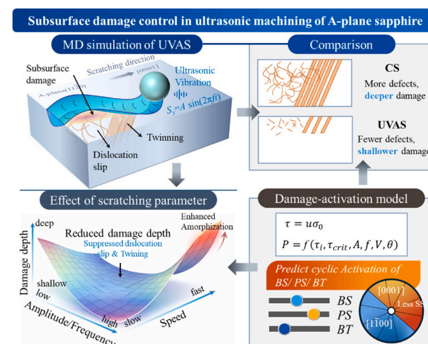

ARTICLE INFO

Keywords:
Ultrasonic vibration-assisted scratching
Molecular dynamics simulation
A-plane sapphire
Subsurface damage mechanism
Slip-twinning damage activation model

ABSTRACT

Sapphire substrates are essential for advanced optoelectronic and power devices, but their extreme hardness and strong elastic-plastic anisotropy readily induce severe subsurface damage (SSD) during conventional machining, limiting wafer-scale yield and device reliability. Although ultrasonic vibration-assisted scratching (UVAS) can reduce forces and damage, the defect-suppression mechanisms on the A-plane and their dependence on vibration parameters and scratching direction remain insufficiently resolved. This paper used molecular dynamics simulations of UVAS to elucidate the coupled roles of vibrational parameters and crystal orientation on dislocation/twinning activity, amorphization, and SSD depth. Results show that UVAS significantly suppresses the formation of dislocation networks and twinning through cyclic unloading, thereby reducing damage depth. However, extremely high frequencies and strain rates promote atomic amorphization and thicken the damage layer. A strong anisotropic response is observed: scratching along the [0001] orientation produces a denser but shallower defect zone along the $[1\bar{1}00]$ orientation. Building on Schmid-type criteria, an ultrasonically modulated damage activation model is developed to reproduce the within-cycle activation/suppression of slip and twinning systems

* Correspondence to: Z. Hu, Institute of Manufacturing Engineering, Huaqiao University, Xiamen, China.
** Correspondence to: X. Xu, Institute of Manufacturing Engineering, Huaqiao University, Xiamen, China.
*** Corresponding author.
E-mail addresses: huzhongwei@hqu.edu.cn (Z. Hu), xpxu@hqu.edu.cn (X. Xu), Z.Wenhan@hud.ac.uk (W. Zeng).

https://doi.org/10.1016/j.jmapro.2026.04.034
Received 29 December 2025; Received in revised form 2 March 2026; Accepted 13 April 2026
Available online 17 April 2026
1526-6125/© 2026 The Society of Manufacturing Engineers. Published by Elsevier Ltd. All rights are reserved, including those for text and data mining, AI training, and similar technologies.

and to provide a predictive framework for parameter selection. By integrating atomistic insights with continuum-scale modeling, the present study provides the first mechanistic guidelines for ultrasonic vibration-assisted processes of anisotropic sapphire.

1. Introduction

Sapphire is indispensable in advanced optoelectronic and power devices, serving as a window material for lasers [1,2], a substrate for GaN-based LEDs [3–5], AlN-based power electronic devices, and a key component in high-frequency radio-frequency modules [6–8]. Among the various crystal orientations, A-plane (11$\overline{2}$0) sapphire is particularly attractive due to its unique thermodynamic and dielectric properties, which are favorable for the heteroepitaxial growth of nonpolar and semipolar nitrides and for the fabrication of high-performance optical windows [9,10]. However, A-plane exhibits higher hardness and elastic modules than other orientations, making it extremely difficult to machine. Conventional sapphire processing relies on multi-abrasive mechanical contact, which not only results in low efficiency but also leads to surface and subsurface fracture and micron-scale cracks [11–13]. These defects severely degrade the mechanical strength and service life of devices. Moreover, as device integration and wafer diameter continue to increase, controlling nanoscale subsurface damage (SSD) on substrate has become a critical bottleneck for improving yield and reliability.

With the continuous advancement of precision machining technologies, the concept of field-assisted processing—combining ultrasonic [14–17], thermal [18–20], electric [21,22], or chemical [23–25] with mechanical material removal [26–28]—has emerged as a key enabling strategy for the efficient, low-damage machining of ultra-hard crystals. Among these methods, ultrasonic vibration-assisted processes have been widely applied for sapphire machining [29–32]. By superimposing one-dimensional or two-dimensional ultrasonic vibration onto conventional machining, periodic separation between the tool and workpiece is achieved. This method reduces the average chip thickness and contact time, thereby lowering cutting forces [33,34], extending tool life [35,36], improving surface finish [37–39], and enlarging the ductile machining regime [40,41]. Experimental studies on ultrasonic vibration-assisted grinding (UVAG) of sapphire experiments have demonstrated that, compared with conventional grinding, the application of ultrasonic vibration can significantly suppress edge chipping, improve surface morphology, and mitigate surface and subsurface cracks [42]. Longitudinal-torsional and multimode ultrasonic configurations further improve surface integrity and roughness, indicating that vibration direction and mode are critical control parameters [43]. At the single-abrasive level, ultrasonic vibration-assisted scratching (UVAS) of sapphire enables more stable chip formation [44,45] and improve scratching quality for wafer dicing and chip separation [46]. Although these macroscopic studies clearly demonstrate the advantages of ultrasonic assistance in sapphire machining, they cannot elucidate how ultrasonic vibration modulates defect nucleation and propagation in the subsurface of specific crystal planes (such as the A-plane), particularly at the nanoscale.

Molecular dynamics (MD) simulation provides a complementary, atomistic approach [47–49] for elucidating the anisotropic deformation and damaging mechanisms of sapphire under scratching. MD simulations of nanoindentation and nano-scratching have revealed a rich spectrum of deformation modes across different crystal planes, including dislocation slip, basal and rhombohedral twinning, and orientation-specific crack initiation [50–53]. These simulations have further quantified how indentation direction and loading depth govern the balance between plasticity and cleavage. Meanwhile, MD studies of ultrasonic vibration-assisted polishing have clarified the effects of high-frequency vibration on force oscillations [54], chip morphology [55], temperature rise, and SSD depth during material removal on the C-plane [56]. Additional MD studies examining UVAS on different sapphire crystal orientations have further highlighted the strong anisotropic response of different planes to ultrasonic assistance [57]. However, these studies have mainly focused on global indicators such as average forces and SSD depth, rather than establishing mechanistic links between vibration parameters, resolved shear/twinning stresses, and the activation of specific defect modes. At present, no study has systematically examined the subsurface defect distribution on the A-plane under ultrasonic vibration-assisted processing, especially the competitive evolution of dislocations and twinning within the vibration cycle.

Significant progress has been made in slip-system activation models during conventional machining conditions. Yuta et al. [58] calculated resolved shear stresses on active slip and twinning systems to investigate crack morphologies and critical depths of cut during the brittle-to-ductile transition. He et al. [59] evaluated slip/twinning activation probabilities to correlate damage mechanisms with the inherent crystal anisotropy of sapphire. Wang et al. [60] employed Schmid and cleavage factors to investigate the plastic deformation and brittle spalling mechanisms of sapphire. Despite these advances, predictive frameworks for SSD at the microscale remain underdeveloped, particularly under ultrasonic vibration-assisted processing. Existing SSD prediction models for UVAG are primarily constructed from kinematic analyses and grinding force models [61–63]. However, these models typically treat sapphire as an elastically isotropic material and do not explicitly link vibration parameters with the activation of specific slip/twinning systems. Therefore, it is necessary to establish a "damage activation" model for ultrasonic vibration-assisted processing that can describe defect

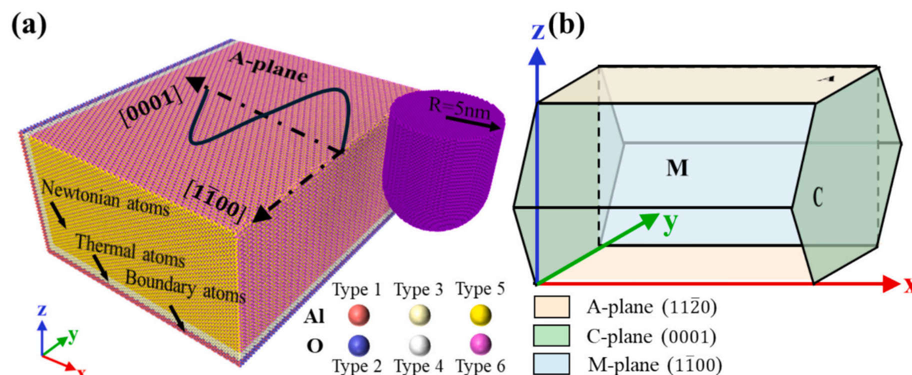

Fig. 1. (a) Atomistic scratching model and (b) crystal orientation of sapphire. The black curves in the diagram represent the movement track of the single grain, and different types of atoms are represented by different colors.

Table 1
Parameters employed in this study.

Parameters	Specimens: sapphire (A-plane)		Indenter: diamond
	[0001]	[1$\bar{1}$00]	
Dimensions (nm)	30 × 30 × 15		Radius: 5
Number of atoms	3,216,780	3,129,840	155,071
Time step (fs)	1		
Temperature (K)	297		
Scratching depth (nm)	5		
Scratching speed (m/s)	60,80,100,120,140		
Amplitude (nm)	1,2,3,4,5		
Frequency (GHz)	8.33,16.67,33.33,66.67,133.3		

nucleation and evolution along individual grain trajectories.

In this work, MD simulations of ultrasonic vibration-assisted single-grain scratching on the A-plane of sapphire were conducted to investigate the influence of vibration parameters and scratching direction on SSD, with particular focus on the formation and competition between dislocations and twinning. Based on conventional crystal slip-activation models, an ultrasonically modulated damage activation model was developed by incorporating ultrasonic kinematic parameters and crystal orientation. This model successfully elucidates the cyclic evolution of individual slip/twinning systems throughout the vibration period. The results offer actionable guidance for optimizing ultrasonic vibration-assisted processes to achieve low-damage, high-efficiency manufacturing of A-plane substrates.

2. MD simulation details

Fig. 1(a) shows the MD model for ultrasonic vibration-assisted single-grain scratching of A-plane. The model comprises a spherical diamond grain and a sapphire workpiece. The sapphire is divided into three distinct regions: (i) a boundary layer with fixed atoms, (ii) a thermostat layer to maintain at a constant temperature to dissipate frictional heat, and (iii) a Newtonian layer where the grain-workpiece interaction occurs. Atoms in these regions are distinguished by different colors for clarity. Fig. 1(b) presents the hexagonal crystal structure of sapphire. The A-plane is constructed by rotating the coordinate system relative to the C-plane, and its crystal directions [0001], [1$\bar{1}$00], and [11$\bar{2}$0] are aligned with the Cartesian x, y, and z axes, respectively. To avoid spurious initial forces, the grain is placed 5 nm to the right of the workpiece, with its spherical center coplanar with the workpiece surface to achieve a constant scratching depth. The simulations are performed using the Large-scale Atomic/Molecular Massively Parallel Simulator (LAMMPS) [64–66]. Periodic boundary conditions are applied in the x and y directions to reduce finite-size effects [67,68]. Interatomic interactions within sapphire (Al—O) are described by Buckingham potential [69,70], whereas the interaction between the diamond (C atoms) and sapphire (Al and O atoms) is modeled using Lennard-Jones 12-6 potential [71,72]. Because different crystal planes exhibit distinct intrinsic stresses, the A-plane is first relaxed for 50 ps under an NPT ensemble to release internal stress. Subsequently, energy minimization and further equilibration are carried out using an NVE ensemble

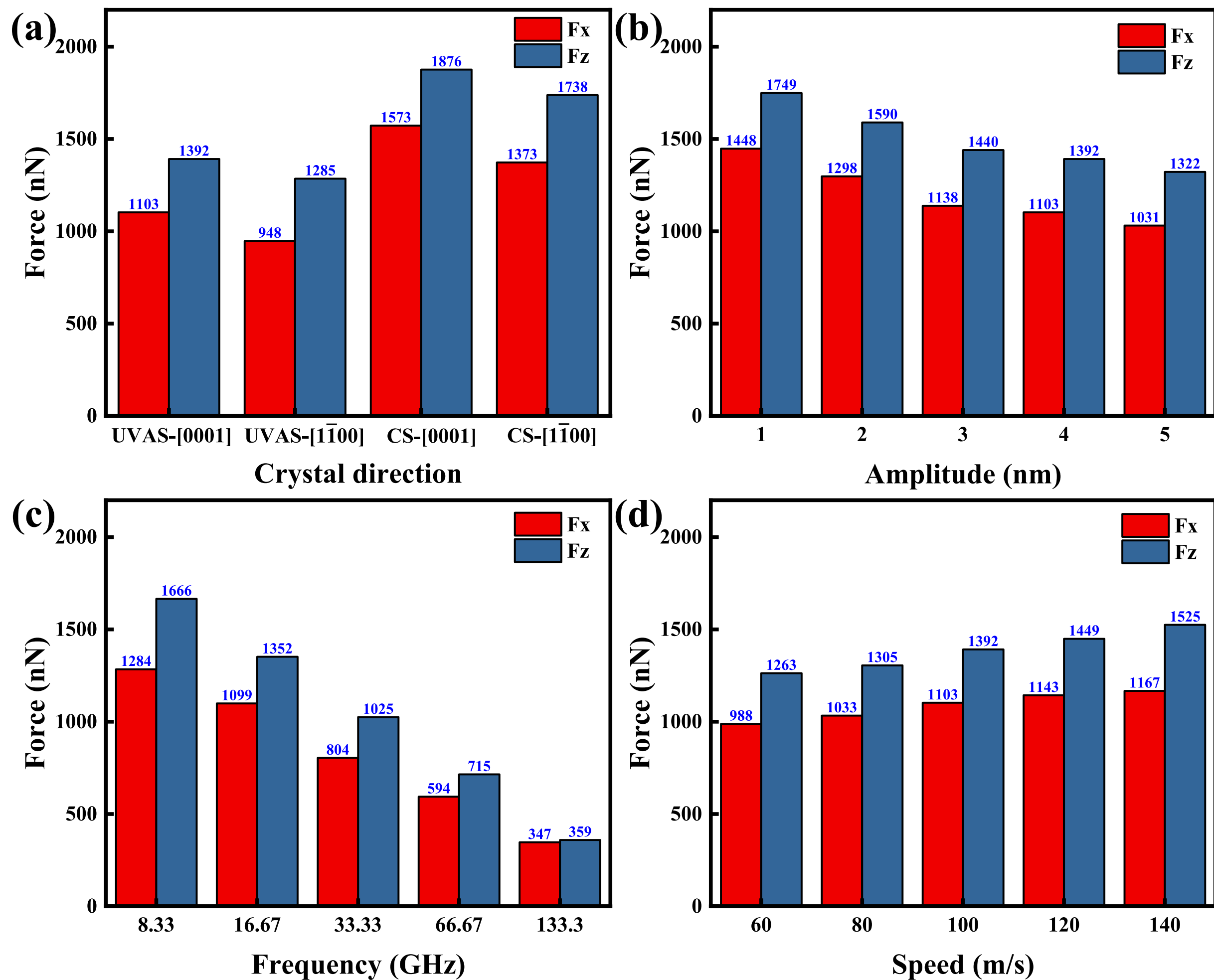

Fig. 2. Effect of ultrasonic vibration process parameters on scratching force: (a) Crystal direction; (b) amplitude; (c) frequency; (d) speed. In all figures, the red bars represent tangential force (Fx) and the blue bars represent normal force (Fz). (For interpretation of the references to color in this figure legend, the reader is referred to the web version of this article.)

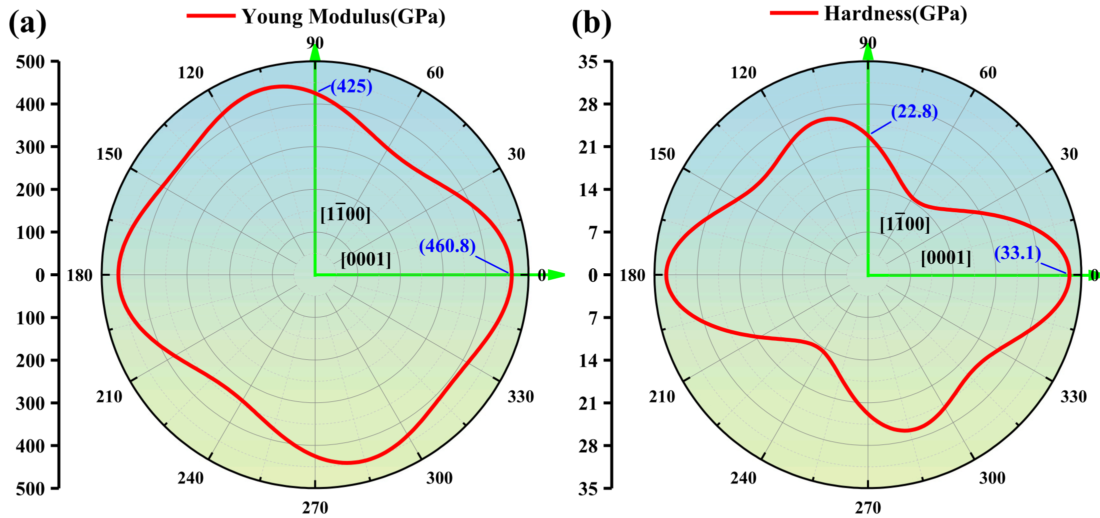

Fig. 3. (a) Young modulus and (b) Hardness along different crystal orientations on A-plane.

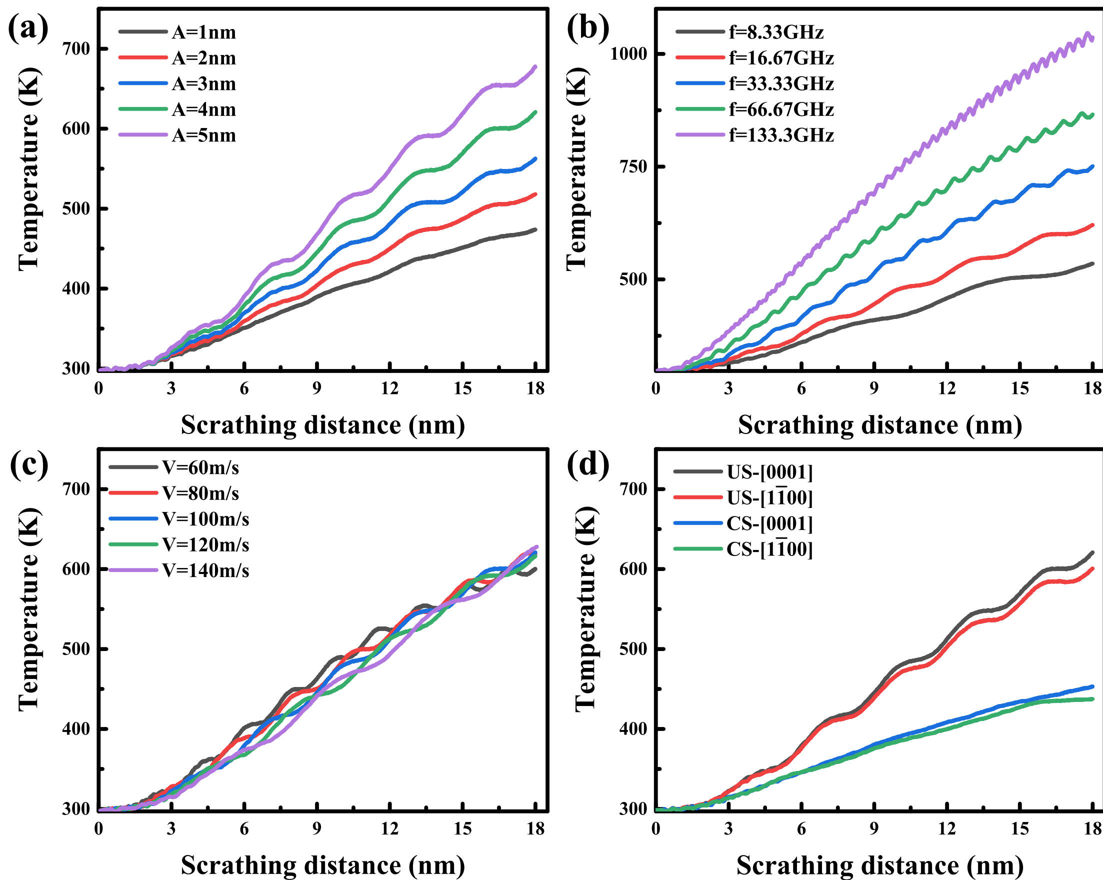

Fig. 4. Contact-zone temperature–distance curves under ultrasonic vibration–assisted nano-scratching: parametric effects of (a) amplitude, (b) frequency, (c) speed, and (d) scratching direction (UVAS vs CS).

combined with a Langevin thermostat [73,74].

The simulations encompass both conventional scratching (CS) and UVAS. In the CS, the grain moves along the x-axis at a constant speed of 100 m/s, with a scratching depth of 5 nm and a total scratching distance of 18 nm. For UVAS, a high-frequency sinusoidal displacement Sy = Asin (2πft) is superimposed along the y-axis. The amplitude A varies as 1, 2, 3, 4, and 5 nm, while the frequency f is set to 8.33, 16.67, 33.33, 66.67, and 133.3 GHz. To further investigate the coupled effects of crystal orientation and ultrasonic vibration, scratching is performed along the [0001] and [1$\bar{1}$00] orientation on the A-plane, respectively. Wear of the diamond grain is neglected throughout the simulations [75,76]. All simulation parameters are summarized in Table 1.

Visualization of the crystal structure and simulation results was performed using OVITO software. Subsurface dislocations and twinning were analyzed by combining the polyhedral template matching (PTM) [77], dislocation extraction algorithm (DXA) [78,79], and common

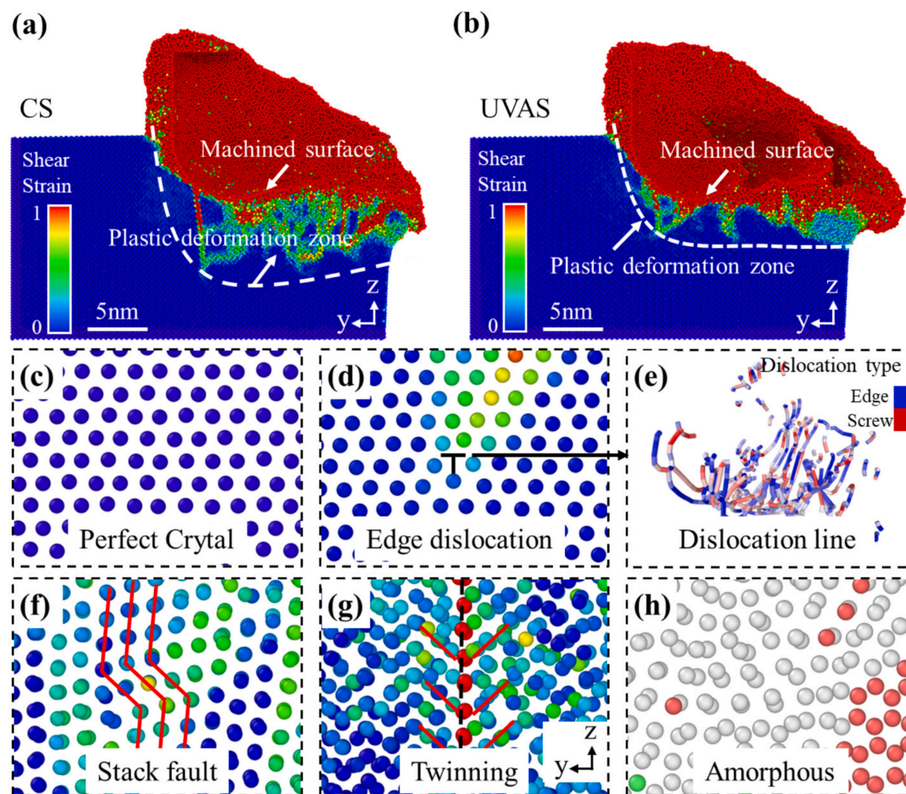

Fig. 5. Plastic deformation zone and typical lattice defects induced by single grain scratching of sapphire: cross-sections of the workpiece colored by atomic shear strain, comparing (a) CS and (b) UVAS; (c) perfect crystal without defects; (d) edge dislocation; (e) three-dimensional dislocation lines colored by character (edge vs. screw); (f) stacking faults composed of partial dislocations; (g) deformation twinning with mirror-symmetric lamellae across the twinning plane; (h) amorphous region where long-range order is destroyed.

neighbor analysis (CNA) [80–82].

3. Results and discussion

3.1. Scratching force

Fig. 2(a) shows the evolution of tangential force (Fx) and normal force (Fz) for CS and UVAS along the [0001] and [$1\bar{1}00$] orientations. All force values correspond to the average forces in the steady stage. Under UVAS, the tool-workpiece contact alternates between loading and partial unloading within each vibration cycle. This intermittent contact reduces the mean load and limits sustained shear traction at the interface, which directly lowers both Fx and Fz. In addition, the oscillatory motion changes the instantaneous relative velocity direction, further dispersing the shear component and preventing continuous stress accumulation. A detailed mechanistic explanation based on the scratching force model is provided in Ref. [83]. As a result, UVAS produces lower mean forces than CS, while the scratching direction has a pronounced effect on the forces. In both CS and UVAS, forces along the [0001] orientation are markedly higher than those along the [$1\bar{1}00$] orientation. This behavior directly reflects the strong mechanical anisotropy of sapphire: Young's modulus and hardness are significantly greater along [0001] orientation than along [$1\bar{1}00$] orientation, as shown in Fig. 3, the data were obtained from theoretical formulas for anisotropic elasticity [84,85].

Fig. 2(b–d) present the influence of amplitude, frequency, and speed on the average tangential force and normal force. Both forces decrease markedly with increasing amplitude and frequency. This reduction stems from two synergistic effects. Larger amplitudes and higher frequencies increase the effective scratching trajectory, enhancing frictional heating. The resulting thermal accumulation (Fig. 4) in the contact region leads to thermal softening of the substrate (i.e., reduced hardness and brittleness), which promotes amorphization and material removal. In addition, increased trajectory overlaps at higher amplitude and frequency leads to repeated removal of already-amorphized material, further lowering scratching resistance. By contrast, both the average tangential and normal forces tend to increase with speed. Higher speed elevates the strain rate at the grain tip, requiring larger cutting forces to remove material. Meanwhile, the effective trajectory length shortens and trajectory overlaps decreases, reducing the proportion of previously amorphized material that is repeatedly removed. As a result, scratching forces progressively increases.

As shown in Fig. 4, the temperature increases monotonically with increasing vibration amplitude and frequency, with frequency exerting the most pronounced effect (the peak temperature exceeds 1000 K). By contrast, when the scratching velocity varies from 60 m/s to 140 m/s, the temperature also increases but only within a relatively small range. In addition, a comparison between ultrasonic vibration–assisted scratching (UVAS) and conventional scratching (CS) indicates that, for both crystallographic directions, UVAS generates substantially higher temperatures than CS. These results support that the temperature rise promotes deformation and structural disordering in the near-surface region, thereby reducing the cutting forces.

3.2. Subsurface damage formation mechanism

Fig. 5 presents a comparative analysis of subsurface deformation and damage in A-plane under CS and UVAS. In both regimes, intense localized strain manifests as shear bands and clusters of high-strain atoms immediately ahead of and beneath the indenter, indicating substantial plastic deformation. The plastically deformed zones are outlined by white dashed lines. Regardless of the processing method, once plastic

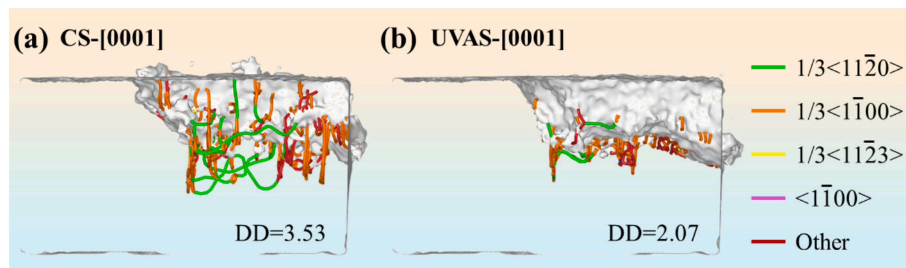

Fig. 6. Effect of ultrasonic vibration on dislocation structures during [0001] orientation scratching: (a) CS; (b) UVAS. Colored lines represent different Burgers vectors. DD represents dislocation density.

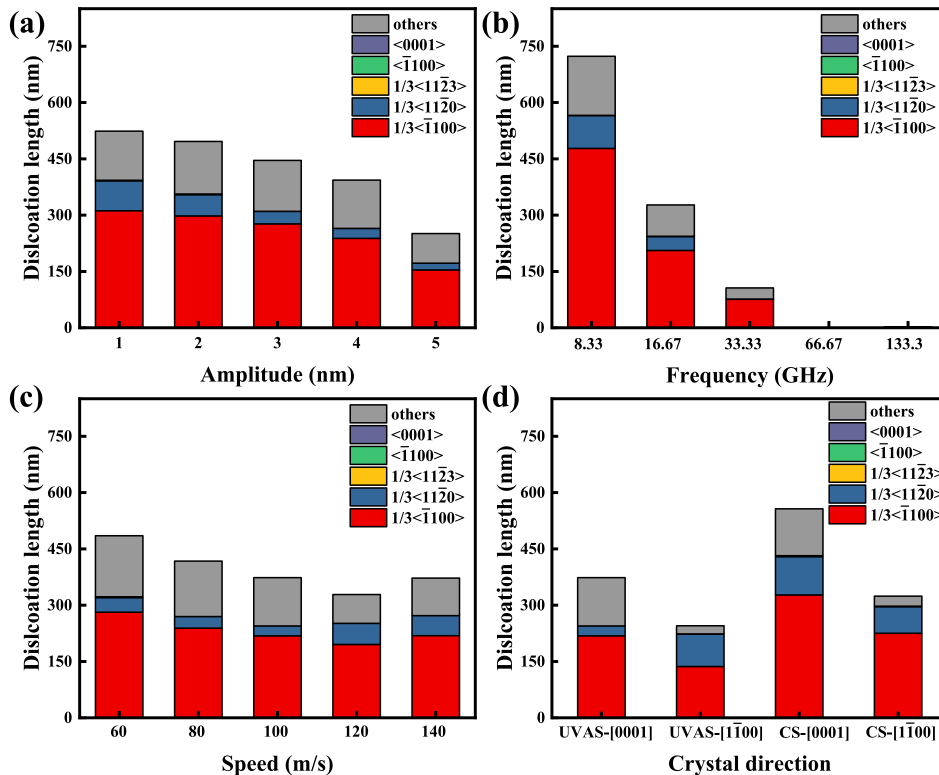

Fig. 7. The dislocation length generated varies with different scratching parameters: (a) Amplitude; (b) Frequency; (c) Speed; (d) Crystal direction. Different colors represent dislocations with different Burgers vectors.

deformation occurs, the machined surface and subsurface inevitably lose their original perfect crystal structure. In the lower-strain regions, plastic deformation is accommodated primarily by dislocation activity. As shown in Fig. 5(d–e), a dense dislocation network consisting of screw, edge, and mixed dislocations forms beneath the scratching. As local stress intensifies, stacking faults emerge, acting as precursors that facilitate the subsequent formation of twinning, as illustrated in Fig. 5 (f–g). At higher strain rates, extensive atomic disorder culminates in amorphization, which mainly occurs the scratch flanks and the shallow near-surface region in direct contact with the grain, as shown in Fig. 5 (h). Under the same nominal conditions, subsurface layer in CS is characterized by deep-penetrating shear bands that propagate preferentially along basal planes. In contrast, the plastically deformed region in UVAS is significantly shallower. This indicates that the efficacy of ultrasonic vibration in mitigating machining-induced damage in sapphire, primarily because the imposed vibration helps to reduce the normal force and thereby suppresses plastic deformation such as basal slip.

3.2.1. Dislocation formation and evolution

Dislocation formation is a primary manifestation of SSD. Fig. 6 shows the dislocation structures generated when a diamond grain scratches along the [0001] orientation on A-plane, with and without ultrasonic vibration assistance. The dislocations are mainly distributed beneath and flanks of the scratching. The dominant dislocation types possess Burger's vectors of $1/3\langle 11\bar{2}0\rangle$ and $1/3\langle 1\bar{1}00\rangle$. The number of dislocations is quantified in terms of dislocation density in the figure. Under CS, the subsurface deformed zone is dominated by a dense and highly entangled dislocation network. In contrast, the subsurface of UVAS generates markedly shorter, shallower, and discontinuous dislocation segments. These observations clearly demonstrate that the application of ultrasonic vibration substantially suppresses both the nucleation and the proliferation of dislocations, thereby significantly mitigating subsurface damage.

Fig. 7(a–c) show the variation length with amplitude, frequency, and speed for different dislocation types. As amplitude increases, the dominant $1/3\langle 1\bar{1}00\rangle$ dislocations and the secondary $1/3\langle 11\bar{2}0\rangle$ dislocations decrease. Notably, the $1/3\langle 11\bar{2}0\rangle$ dislocations almost disappear at large amplitude. The total dislocation line length shows a similar

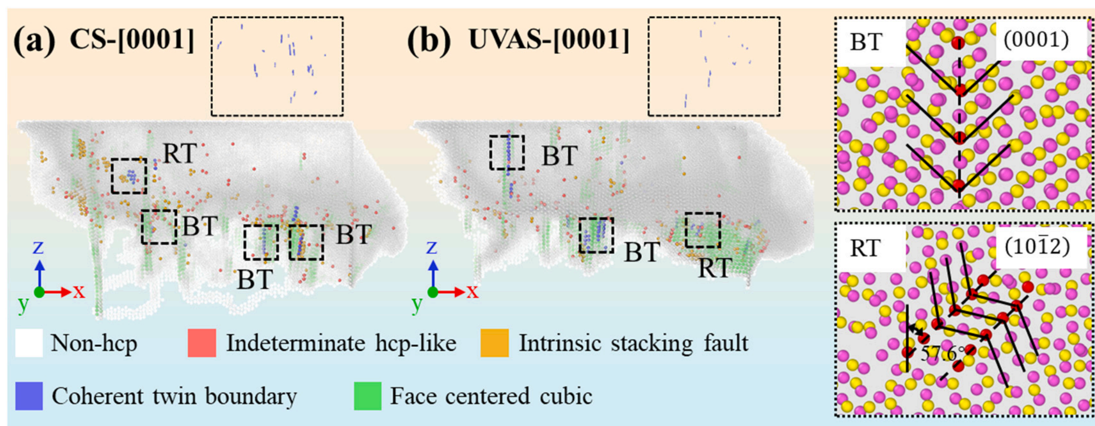

Fig. 8. The distribution and type of twinning generated in sapphire during single grain scratching along the [0001] orientation: (a) CS and (b) UVAS. The results obtained by common neighbor/polyhedral template analysis. Colored atoms denote different local structures.

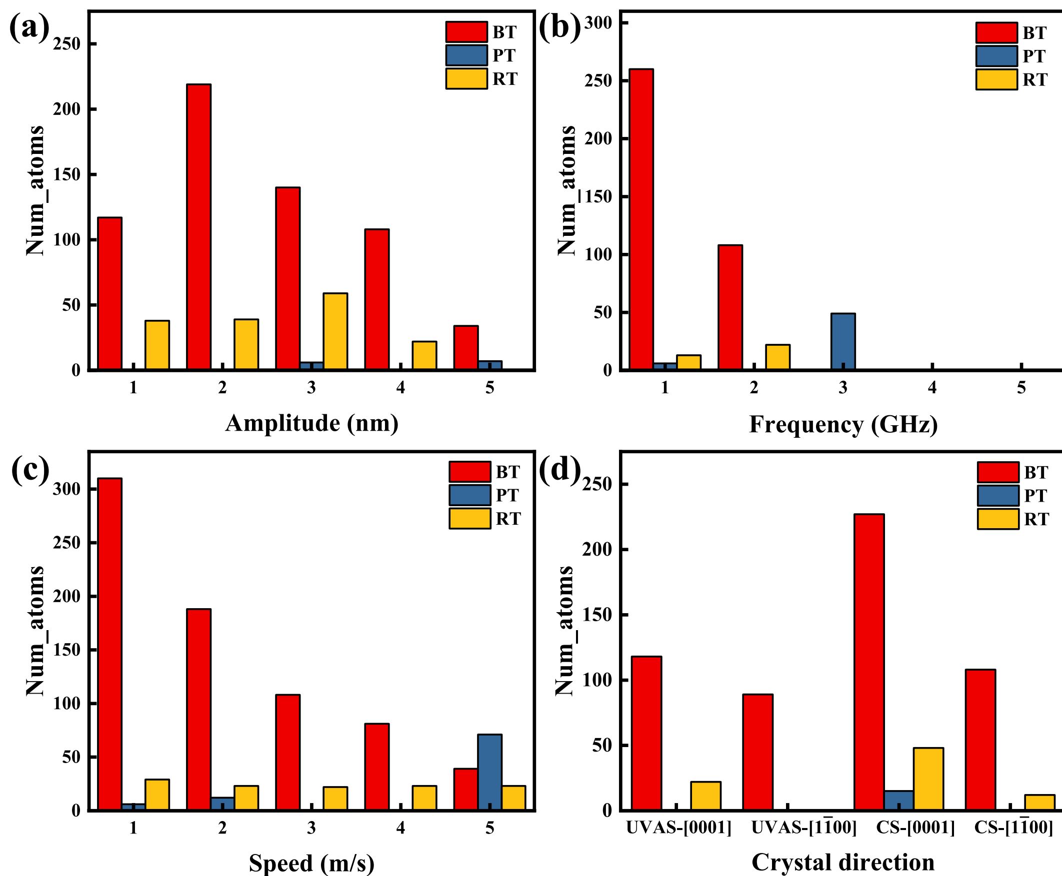

Fig. 9. The number of different twinning atom types generated varies with different scratching parameters: (a) Amplitude; (b) Frequency; (c) Speed; (d) Crystal direction. Red bars denote basal twinning (BT), blue bars prismatic twinning (PT), and yellow bars rhombohedral twinning (RT). (For interpretation of the references to color in this figure legend, the reader is referred to the web version of this article.)

trend. Increased frequency also causes a rapid decrease in dislocation line length for all types. When the frequency exceeds ~66.7 GHz, dislocation activity in the observation area essentially disappears, indicating that ultra-high frequency vibrations significantly enhance the dislocation annihilation process. This behavior is consistent with a tendency toward localized amorphization induced by the high strain rates associated with high-frequency vibration. Overall, increasing amplitude and frequency significantly reduces the scratching forces, making the resolved shear stress on the active slip system insufficient to maintain the continuous nucleation and slip of dislocations. In contrast, with increasing speed, the total dislocation line length first decreases and then increases. Below a critical threshold, fewer vibration cycles occur per unit scratching distance, reducing chances for dislocation generation and slip. Beyond a critical speed, however, the local strain rate rises sharply and elevates the transient shear stress, thereby reactivating dislocation activity. The resulting stronger impact loading not only rapidly activates the initially dominant slip systems but also triggers additional slip systems, enhancing dislocation emission from defect sites and a subsequent rise in dislocation density. Moreover, dislocation formation also displays pronounced crystal anisotropy, as shown in

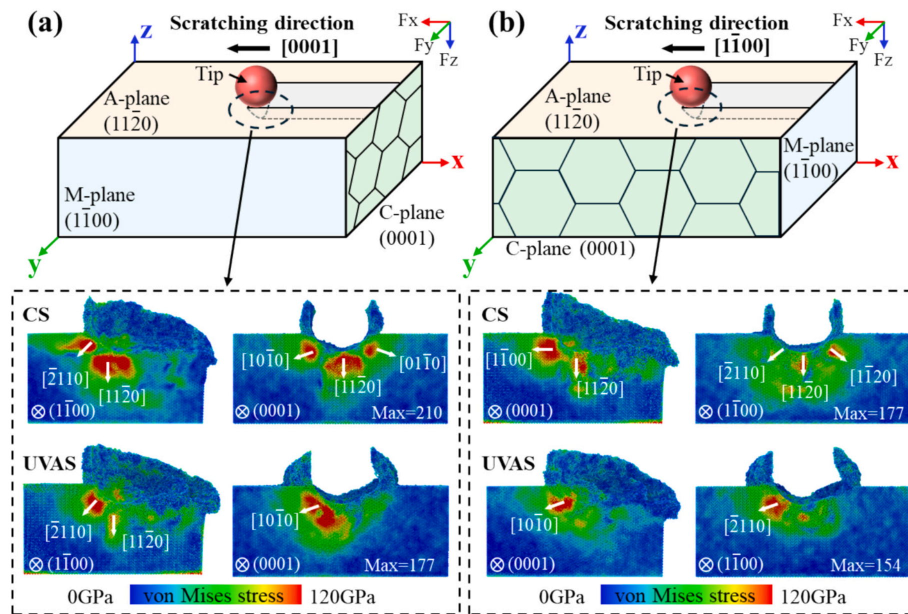

Fig. 10. Anisotropic von Mises stress fields along (a) [0001] orientation and (b) [1$\bar{1}$00] orientation during scratching of A-plane. The top schematics show the scratching along different directions, while cross-sections are taken to examine the stress field beneath the groove. The colored maps in the lower panels present the von Mises stress, where red denotes high stress concentrations and the crystal directions in each section are indicated. (For interpretation of the references to color in this figure legend, the reader is referred to the web version of this article.)

Fig. 7(d). Along the [0001] orientation, significantly more 1/3⟨1$\bar{1}$00⟩ dislocations are generated than along [1$\bar{1}$00] orientation, irrespective of whether ultrasonic vibration is applied. For CS, the evolution of 1/3⟨11$\bar{2}$0⟩ dislocations are like that of 1/3⟨1$\bar{1}$00⟩. However, under UVAS, the length of 1/3⟨11$\bar{2}$0⟩ dislocations along [0001] orientation become markedly shorter than along [1$\bar{1}$00] orientation. This behavior is related to the different activation barriers of the corresponding slip systems, which will be discussed in detail in Section 4.2. These results indicate that judicious selection of scratching direction, in combination with optimized ultrasonic parameters, offers an effective strategy for minimizing subsurface damage during precision machining of A-plane sapphire.

3.2.2. Twinning nucleation

Twinning analysis is critical for guiding process optimization and minimizing subsurface machining damage. Fig. 8 illustrates the role of ultrasonic vibration in activating specific twinning modes during scratching along the [0001] orientation and compares it with CS. Basal twinning (BT) dominates in both cases. In CS, sustained high hydrostatic pressure coupled with steady resolved shear stress on the basal plane promotes the formation of thick, continuous twinning boundaries. In contrast, under UVAS, the BT layers become noticeably shallower and more diffuse, with fewer and shorter twinning boundaries. This suppression originates from the reduction in average normal force after ultrasonic application. The dynamic unloading-reloading process prevents some of the scratching stress from exceeding the threshold for BT, thus interrupting the continuous nucleation of the twinned lattice. Furthermore, the lateral motion in UVAS generates lateral shear components that activate BT on both flanks of the scratching groove–a feature rarely observed in CS. Rhombohedral twinning (RT) is only rarely observed and appear exclusively under more severe local stress conditions.

Fig. 9(a–c) show the influence of vibration parameters and speed on the number of different twinning atom types. The different twinning types are distinguished. Consistent with Fig. 7, BT dominates under all conditions, confirming that the stress state on the A-plane favors this lowest-energy twinning mode. However, the atom numbers of PT and RT remain very small and are therefore excluded from further discussion. As the amplitude increases, the atom numbers of BT first rise and then decrease. The initial increase is attributed to the expansion of the plastically deformed region and the periodic enhancement of lateral shear, which makes BT energetically more favorable. With further increase in amplitude, the progressive reduction in both normal and tangential forces lowers the resolved shear stress and hydrostatic pressure, shifting deformation toward dislocation-mediated plasticity and thereby diminishing the effective driving force for twinning nucleation. At the lowest frequency (8.33 GHz), the atom numbers of BT reach their maximum. As frequency increases, it decreases monotonically and approaches zero above ~66.7 GHz. At low frequencies, the contact point between the grain and the substrate experiences relatively long loading–unloading time per cycle, allowing cyclic normal and shear stresses to act sufficiently on the basal plane and thus promote the nucleation and thickening of BT. Higher frequencies accelerate cyclic loading, promoting direct shear-induced amorphization over coordinated atomic rearrangement into coherent twinning, thereby suppressing BT formation. The atom numbers of BT decrease monotonically as speed rises from 60 m/s to 140 m/s. Higher speed shortens grain-subsurface interaction time per vibration cycle, making dislocation-mediated plasticity more competitive and leaving less time for the nucleation, growth, and thickening of BT. At the same time, the high tangential shear stresses at high speed favor the activation of prismatic twinning systems, which explains the sudden increase in PT.

UVAS-induced twinning exhibits strong orientation dependence, as shown in Fig. 9(d). The atom numbers of BT generated during scratching along [0001] orientation consistently exceeds that along [1$\bar{1}$00] orientation. Under CS, the normal force generated along the [0001] orientation drives larger resolved shear stresses on multiple crystal directions of the basal plane than along [1$\bar{1}$00] orientation, as illustrated in Fig. 10. While applying ultrasonic vibration reduces the effective driving force for BT, it introduces an additional lateral shear component, which is beneficial for the formation of BT in the transverse direction. In addition, the periodic release of contact stress under ultrasonic vibration decreases both the magnitude and duration of the effective twinning driving force, which suppresses overall twinning nucleation.

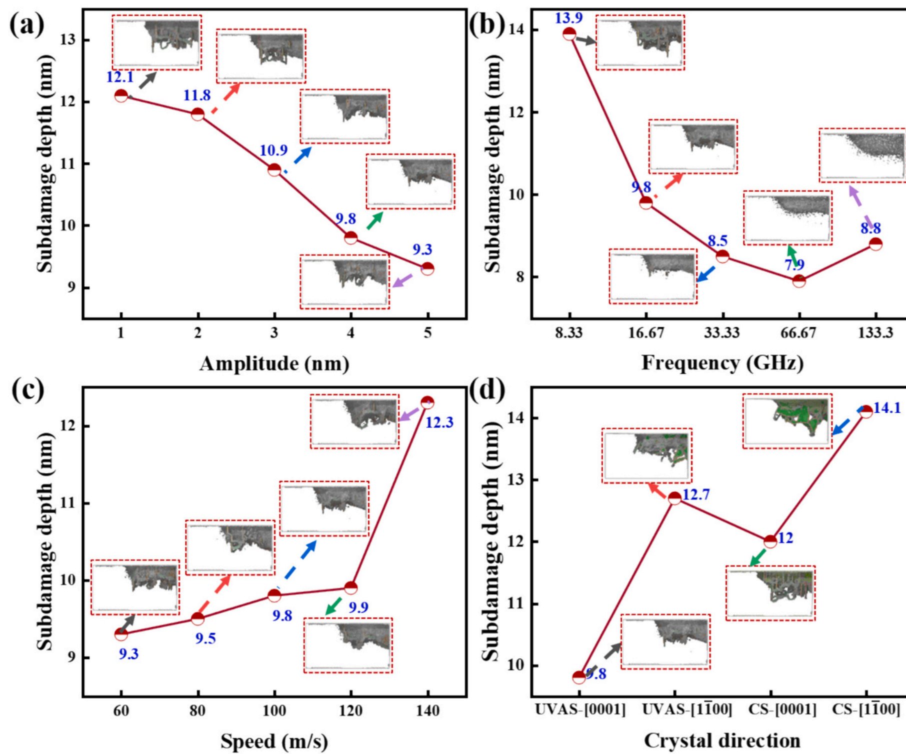

Fig. 11. The subsurface damage varies with different scratching parameters: (a) Amplitude; (b) Frequency; (c) Speed; (d) Crystal direction. Each red point is annotated with the measured SSD depth and paired with a typical cross-sectional micrograph. (For interpretation of the references to color in this figure legend, the reader is referred to the web version of this article.)

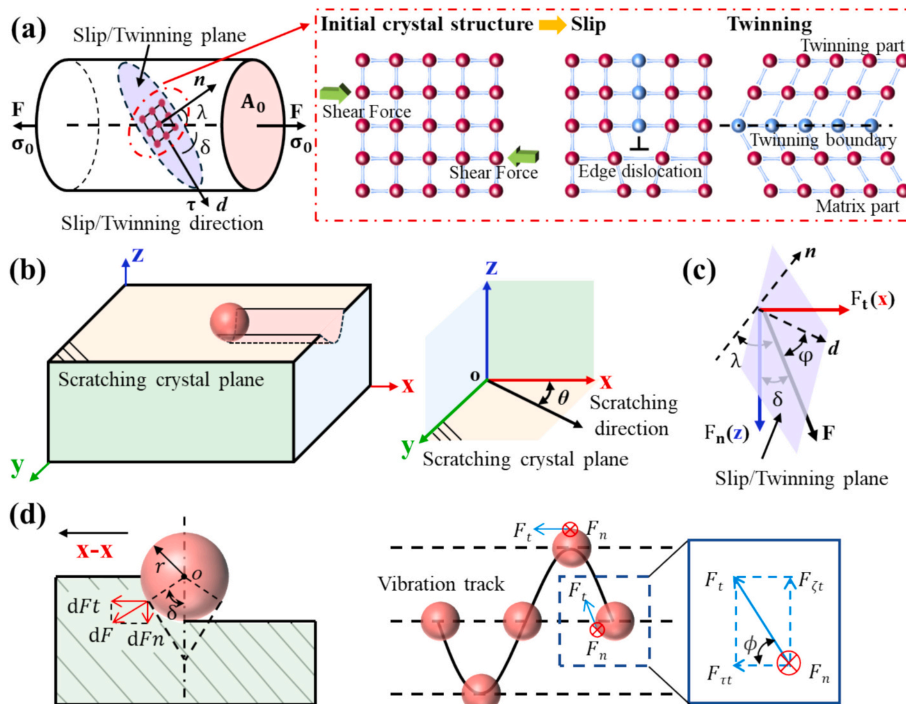

Fig. 12. Schematic of the slip/twinning activation model for ultrasonic vibration-assisted scratching: (a) slip/twinning formation; (b) the geometric relations between the scratching plane and the scratching direction; (c) the geometric relationship between the slip/twinning plane, the slip/twinning direction, and the force; (d) cross-section diagram of partial contact between grain and workpiece.

3.2.3. Subsurface damage depth

Fig. 11 shows the variation of SSD depth beneath scratching formed on the A-plane using UVAS, as a function of vibration parameters and crystal orientation. The SSD depth is quantified as the maximum vertical distance from the initial free surface to the deepest damaged atoms. The dashed boxes in the figure represent snapshots of the corresponding

Table 2
Slip/twinning systems of sapphire for the structural unit cell [89,90].

Slip/twinning system	Miller-Bravais indices	Critical shear stress $\tau_i^{crit}/\min\tau_i^{crit}$
Basal slip (BS)	$\{0001\}\langle 11\bar{2}0\rangle$	1.35
Prismatic slip (PS)	$\{11\bar{2}0\}\langle 1\bar{1}00\rangle$	1
Rhombohedral slip (RS)	$\{01\bar{1}2\}\langle 01\bar{1}\bar{1}\rangle$	2.718
Basal twinning (BT)	$\{0001\}\langle 1\bar{1}00\rangle$	1
Rhombohedral twinning (RT)	$\{1\bar{1}02\}\langle 1\bar{1}0\bar{1}\rangle$	1

damage layers. The SSD depth decreases monotonically with increasing amplitude, from ~12.0 nm to 9.3 nm. The snapshots reveal that at low amplitudes, the plastic zone is relatively thick and rough, with a pronounced downward "root" extending into the substrate. Higher amplitudes confine damage to a thinner, smoother near-surface layer. This result can be attributed to the reduction in normal and tangential forces, causing stress release to tend to occur more readily at the shallow, near-surface via shear deformation. The SSD depth exhibits a typical U-shaped response with frequency. It rapidly drops from 13.9 nm to 7.9 nm, then rises slightly to 8.8 nm at 133.3 GHz. Higher frequencies mean more vibration cycles per unit scratching distance and shorter effective loading times per cycle. This repeated process inhibits the nucleation and slips of some dislocations, thereby reducing the damaged depth. When the frequency rises further to ultra-high levels, however, the material cannot undergo a full plastic response within each extremely short cycle, promoting localized amorphization and causing the SSD to rebound. With increasing speed, the SSD depth remains relatively low in the range 60–120 m/s (≈9.3–9.9 nm), but rises sharply at the highest speed (≈12.3 nm). Higher speeds transition the grain-workpiece interaction toward impulsive loading, elevating instantaneous normal stress, shear stress, and strain rate. This change causes dislocations to slip more sufficiently and penetrate deeper into the material, thereby aggravating subsurface damage. For CS, the SSD depth along [0001] orientation is 12.0 nm, which is notably smaller than the 14.1 nm observed along $[1\bar{1}00]$ orientation. Under UVAS, a corresponding trend is observed, but the SSD depth is significantly reduced. This indicates that ultrasonic vibration effectively mitigates subsurface damage while exhibiting a significant orientation effect.

4. Ultrasonically modulated damage evolution model

4.1. Development of a damage-evolution model for UVAS

As discussed in Section 3.2, subsurface damage in sapphire is primarily governed by slip on specific crystal planes and twinning nucleation. Existing damage-activation models have been developed mainly for CS under quasi-static loading and a corresponding framework for UVAS has not yet been established. Therefore, in this section, we extend

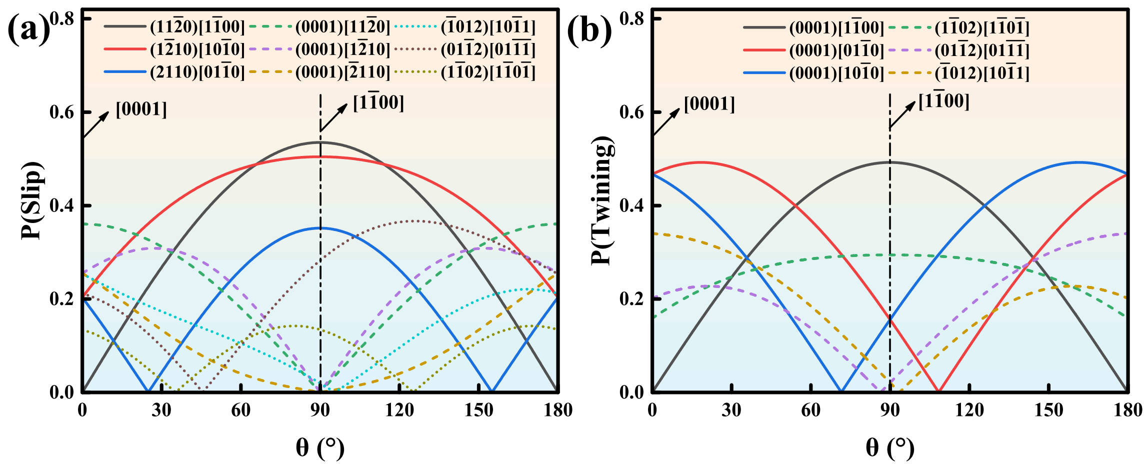

Fig. 13. Orientation-dependent activation of slip and twinning systems on A-plane sapphire. Higher *P*-values indicate lower kinetic barriers and thus greater ease of activation for the corresponding deformation mode.

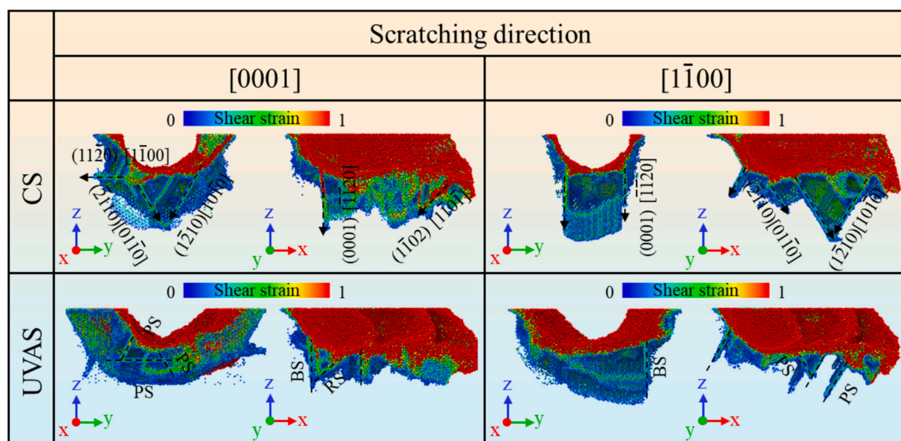

Fig. 14. The subsurface shear-strain distributions and dominant slip systems for different scratching directions with and without ultrasonic vibration. For each case, cross-sections on characteristic planes are colored by atomic shear strain.

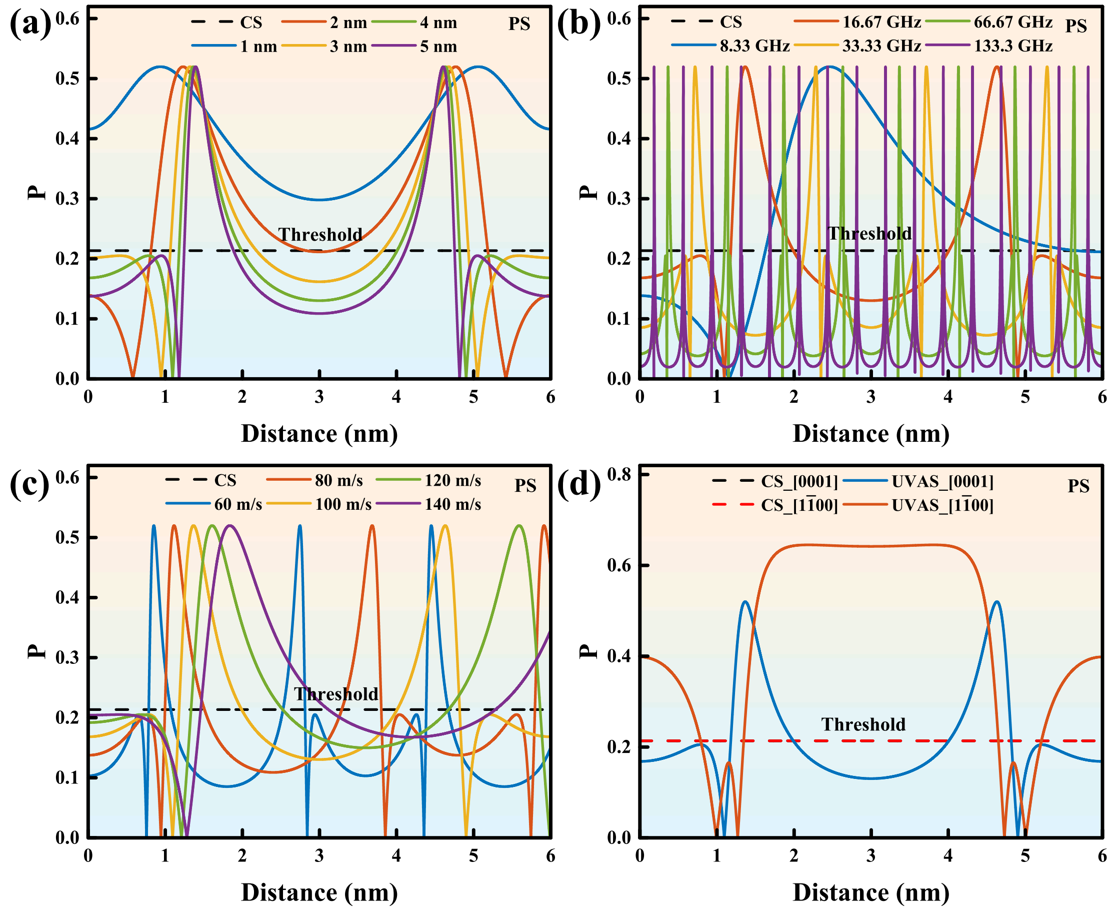

Fig. 15. Effect of ultrasonic parameters and scratching direction on the activation of PS: (a) Amplitude; (b) Frequency; (c) Speed; (d) Crystal direction. A horizontal black dashed line marks the critical threshold for PS activation, determined from the first appearance of PS dislocations in MD simulations.

the classical crystal slip/twinning activation framework by incorporating the oscillatory stress field characteristic of UVAS. The resulting ultrasonically modulated damage-activation model describes defect evolution as a function of a single grain trajectory. The aim is to provide the necessary theoretical foundation for shifting damage control in sapphire from empirical, trial-and-error parameter tuning to mechanism-guided optimization.

Under CS, the evolution of damage induced by slip deformation and twinning nucleation under scratching stress has already been elucidated, as shown in Fig. 12(a). Here, the average compressive stress σ_0 acting normal to the effective contact area A_0 generates a maximum resolved shear stress τ on active slip/twinning systems that drive dislocation slip and twinning when it exceeds the orientation- and pressure-dependent critical value. Their relationship is given by [86]:

$$\tau = u^*\sigma_0,$$

where u is the Schmid factor, which can be expressed as [87],

$$u = \cos\lambda^*\cos\varphi,$$

where λ is the angle between the tensile force F and the normal n to the slip/twinning plane, and φ is the angle between F and the slip/twinning direction d.

To quantitatively assess the activation propensity of individual deformation systems, Nowak et al. [88] introduced a plastic deformation parameter P. For the i-th slip/twining system, P_i is defined as:

$$P_i = \frac{u_i^*\min\tau_i^{crit}}{\tau_i^{crit}}$$

where τ_i^{crit} is the critical resolved shear stress of the i-th slip system, and $\min\tau_i^{crit}$ is the minimum critical resolved shear stress among all slip systems. The critical shear stress parameters for the various slip/twinning systems in sapphire are summarized in Table 2.

To better understand the influence of crystal orientation on scratching-induced damage, a Cartesian coordinate system is established for scratching, as shown in Fig. 12(b). The A-plane surface is perpendicular to the z-axis, while the nominal scratching direction lies in the xy-plane. The [0001] orientation is fixed along the x-axis, and the angle θ between the scratching direction and [0001] is introduced as the orientation parameter. Thus, $\theta = 0^\circ$ corresponds to scratching along [0001] orientation, and $\theta = 90^\circ$ corresponds to scratching along [1$\bar{1}$00] orientation. Fig. 12(c) illustrates the geometric relationship between force **F** and the slip/twinning systems. Under varying scratching conditions (including crystal direction θ, normal force F_n, and tangential force F_t), the propensity for plastic deformation via slip/twinning is encapsulated in a unified activation parameter $P_i(\theta)$, defined as [91]:

$$\begin{cases} P_i(\theta)=\dfrac{\left[(\cos\theta^*\vec{x}+\sin\theta^*\vec{y}-r^*\vec{z})^*\vec{n_i}\right]\left[(\cos\theta^*\vec{x}+\sin\theta^*\vec{y}-r^*\vec{z})^*\vec{d_i}\right]}{\left|(\cos\theta^*\vec{x}+\sin\theta^*\vec{y}-r^*\vec{z})\right|^2*\tau_i^{crit}\Big/\min\tau_i^{crit}} \\ r=\dfrac{F_n}{F_t} \end{cases}$$

In axial ultrasonic vibration-assisted scratching, the scratching stress acting on a single grain are denoted as follows [83]:

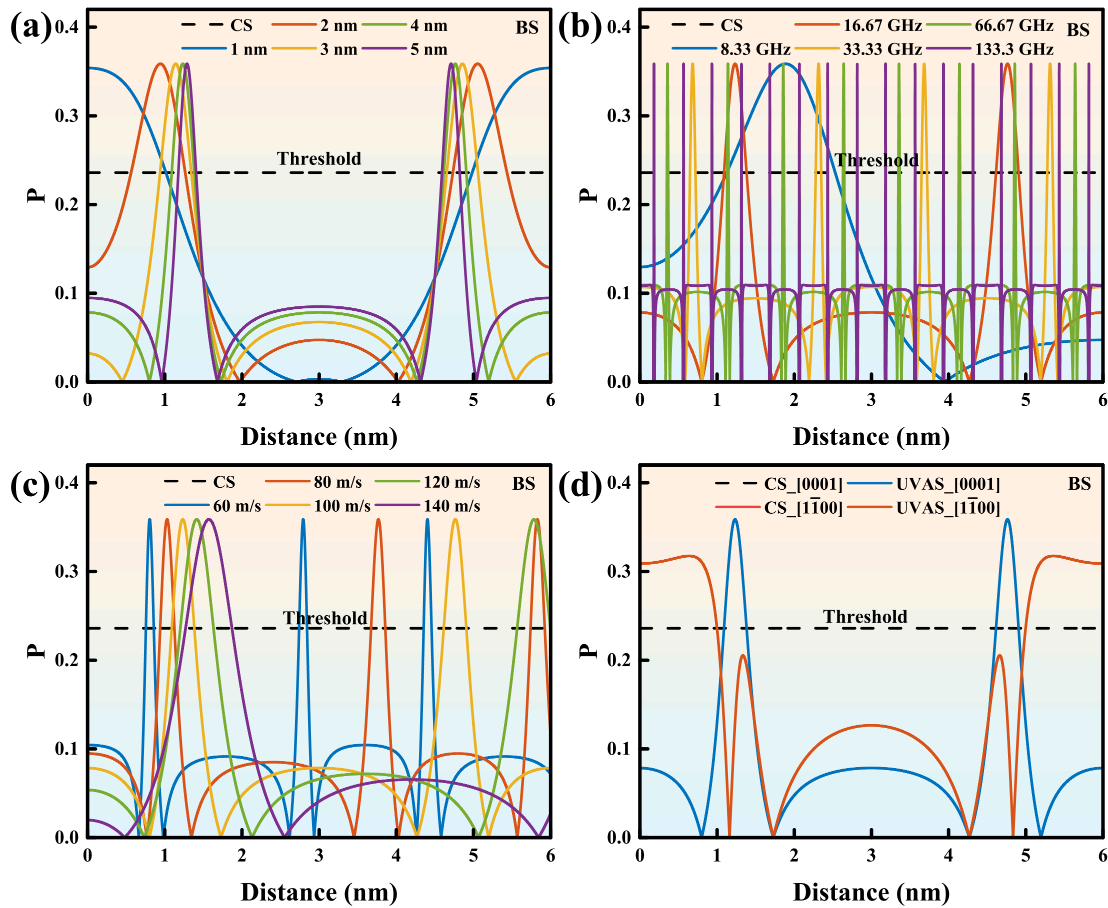

Fig. 16. Effect of ultrasonic parameters and scratching direction on the activation of BS: (a) Amplitude; (b) Frequency; (c) Speed; (d) Crystal direction. A horizontal black dashed line marks the critical threshold for BS activation, determined from the first appearance of BS dislocations in MD simulations.

$$\begin{cases} F_{\tau t}' = \left(\frac{\pi}{2}F_p r^2\left[\frac{1}{3}\left(\cos\delta\right)^3 - \cos\delta + \frac{2}{3}\right]\right)\cos\phi \\ F_{\zeta t}' = \left(\frac{\pi}{2}F_p r^2\left[\frac{1}{3}\left(\cos\delta\right)^3 - \cos\delta + \frac{2}{3}\right]\right)\sin\phi \\ F_n' = \frac{2}{3}F_p r^2(\sin\delta)^3\cos\phi \\ \phi = \arctan\left(\frac{2\pi Af\cos(2\pi ft)}{V_s}\right) \end{cases}$$

where $F_{\tau t}'$, $F_{\zeta t}'$, and F_n' represent the tangential, axial, and normal forces, respectively. Under the UVAS, the motion direction of grain deviates from the nominal scratching direction by an angle ϕ, as illustrated in Fig. 12(d).

4.2. Anisotropy effect on damage evolution induced by crystal-plane slip/twinning

Fig. 13 presents the predicted activation of slip/twinning systems beneath scratching on A-plane under CS, as calculated using the crystal damage-activation model. As shown in Fig. 13(a), scratching along the [0001] orientation activates the {0001} ⟨11$\bar{2}$0⟩, {11$\bar{2}$0} ⟨1$\bar{1}$00⟩, and {01$\bar{1}$2} ⟨2$\bar{1}\bar{1}$0⟩ slip systems. In contrast, scratching along [1$\bar{1}$00] orientation mainly activates the {11$\bar{2}$0} ⟨1$\bar{1}$00⟩ system and only marginally engages the {01$\bar{1}$2}⟨01$\bar{1}\bar{1}$⟩ system. Because the P-value for slip systems such as (1$\bar{1}$02) [1$\bar{1}$0$\bar{1}$] is much lower than that of the other active slip systems. Moreover, the P-value for the {11$\bar{2}$0} ⟨1$\bar{1}$00⟩ system is higher along [1$\bar{1}$00] orientation than along [0001] orientation, facilitating deeper penetration of prismatic slip (PS) and resulting in greater SSD depth, as shown in Fig. 14. Along [0001] orientation, activation of multiple competing slip systems generates a dense, highly entangled dislocation network in which mutual interactions impede long-range slip, thereby confining damage to a shallower region.

The orientation dependence of twinning activation is shown in Fig. 13(b). BT consistently exhibits the highest nucleation parameter in both orientations, confirming its dominance. Although the overall BT activation levels are similar, scratching along [0001] orientation activates two symmetrically equivalent variants—(0001) [10$\bar{1}$0] and (0001) [01$\bar{1}$0]—whereas along [1$\bar{1}$00] orientation only (0001) [01$\bar{1}$0] is favorably oriented. RT shows higher activation propensity along [0001] orientation than along [1$\bar{1}$00] orientation. These predictions align with the simulation observation in Fig. 9(d) that twinning atom numbers are higher when scratching along [0001] orientation.

During UVAS, the evolution of *P*-value for the {11$\bar{2}$0} ⟨1$\bar{1}$00⟩ (PS) system with different conditions is shown on Fig. 15. The curves report the variation of P with scratching distance over one complete vibration cycle, and the value at which PS first activates under CS is taken as the threshold. In the CS case, PS remains stably activated, as indicated by the horizontal black dashed line. When P lies above this line, the PS system is active. Conversely, when *P*-value falls below it, PS is effectively suppressed. When the amplitude is 1 nm, P-value fluctuates but remains above the threshold, indicating that PS remains continuously active throughout the entire cycle. As the amplitude increases, P-value gradually falls below the threshold in the central portion of the cycle, with only a brief over-threshold occurring near the turning point (maximum normal force). This suggests that higher amplitude suppresses PS by markedly shortening the cumulative time above the activation

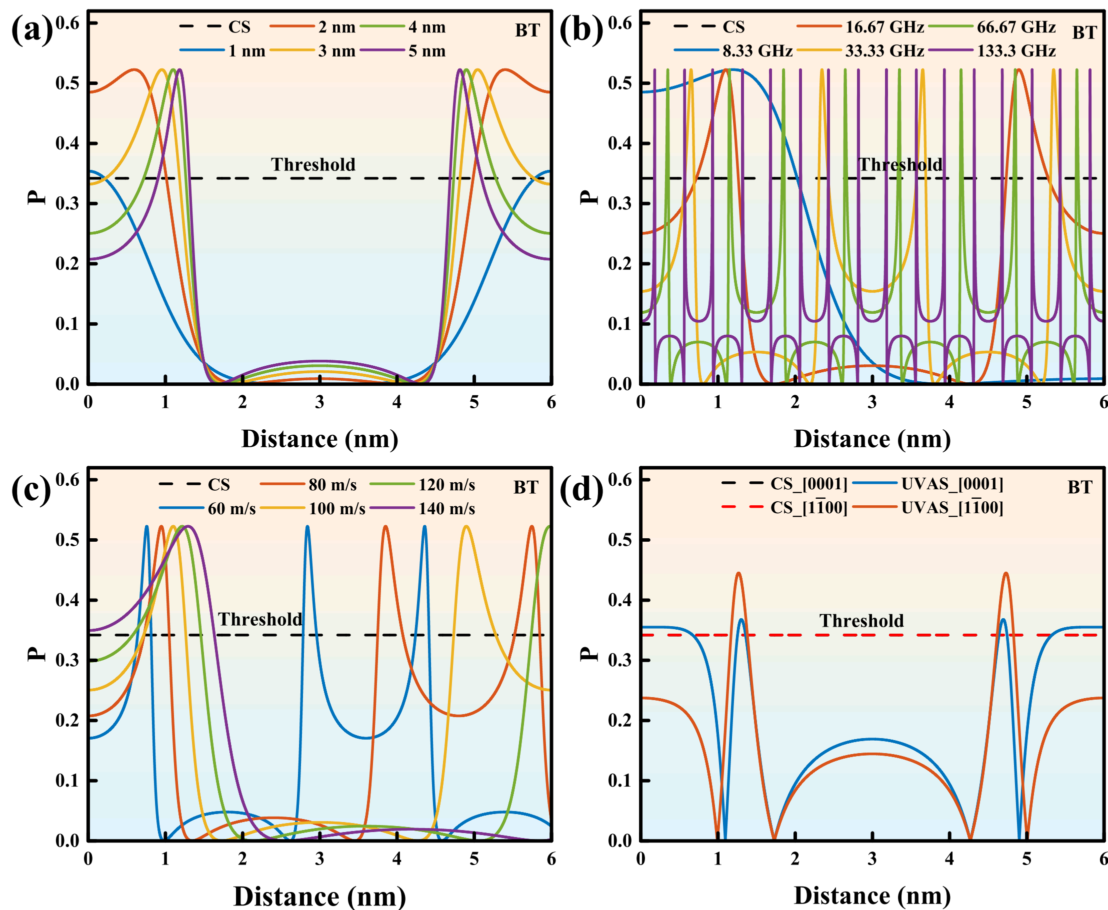

Fig. 17. Effect of ultrasonic parameters and scratching direction on the activation of BT: (a) Amplitude; (b) Frequency; (c) Speed; (d) Crystal direction. A horizontal black dashed line marks the critical threshold for BT activation, determined from the first appearance of BT dislocations in MD simulations.

threshold. Fig. 15(b) reveals the effect of frequency on P-value. At 8.33 GHz, the P curve forms a broad over-threshold peak over most of the cycle, causing continuous activation for PS. With increasing frequency, the over-threshold region shrinks rapidly, and P-curve changes from a broad peak to multiple sharp narrow peaks, meaning that the activation time window of PS is significantly shortened. The sharp reduction in the fraction of the activation interval explains why PS almost completely disappear at high frequencies. Changing the scratching speed alters the width of the above-threshold segments, but the overall level of *P*-value increases with velocity, as shown in Fig. 15(c), confirming the monotonic strengthening effect of velocity on PS-related damage. Strong orientation dependence is evident in Fig. 15(d). When scratching along [1$\bar{1}$00] orientation, P-value remains above the threshold for almost the entire cycle, forming a broad plateau that sustains continuous activation of PS. By contrast, along [0001] orientation, PS is only intermittently activated and with markedly lower magnitude. This directly explains the pronounced orientation anisotropy of PS and SSD depth. The BS system exhibits identical parametric trends, as shown in Fig. 16.

Fig. 17 shows the variation of P for the BT system as a function of scratching distance over one ultrasonic vibration cycle. The threshold of BT is defined in the same way as for the BS/PS systems. At small amplitudes, BT is activated only near the beginning and end of the cycle. As the amplitude increases, both the peak of *P*-value and the over-threshold interval expand, leading to an increase in the number of twinning atoms. Notably, at larger amplitudes, the peak of P-value remains unchanged, whereas over-threshold duration progressively shortens. This characteristic explains the observed trend of the number of BT atoms—initial increase followed by decrease. Although increased frequency triggers BT nucleation more frequently, the over-threshold duration is shorter, leaving insufficient time for twinning to nucleation. Consequently, the total number of BT atoms decreases and eventually vanishes at high frequencies. The effect of scratching speed shows a contradictory trend. The theoretical model predicts a wider over-threshold interval at higher speeds, yet the MD simulations show a persistent reduction in the number of BT atoms. This mismatch likely reflects limitations of the theoretical expression, which does not explicitly account for the time required for twinning nucleation and does not fully capture speed-induced changes in strain rate. In addition, changing the scratching direction modifies the Schmid factor of BT. Although the peak of P-value is higher along [1$\bar{1}$00] orientation than [0001] orientation, the over-threshold duration is markedly longer along [0001] orientation, which is more favorable for sustained BT nucleation and growth. This is consistent with the MD results showing the higher number of twinning atoms observed along [0001] orientation in MD simulations.

Overall, the model's predictions align closely with the defect evolution trends derived from MD simulations, validating its utility for mechanism-guided optimization of UVAS parameters.

5. Conclusion

In conclusion, this study combines atomic-scale simulations with a newly proposed ultrasonic-modulated damage activation model to elucidate the subsurface damage mechanisms of A-plane sapphire during ultrasonic vibration-assisted scratching. The effects of scratching parameters and crystal orientation on damage depth are systematically analyzed. The main conclusions are as follows:

(1) Compared with conventional scratching, UVAS significantly mitigates subsurface damage. The primary mechanism is that the high-frequency unload-reload cycles reduce the normal and tangential forces, thereby suppressing dislocation slip, and limiting twinning nucleation.
(2) Although increasing the vibration parameters (amplitude and frequency) and the scratching speed effectively suppresses the formation of dislocations and twinning, the associated high frequency and high strain rate promote the generation of amorphous atoms, thereby exacerbating damage-layer depth.
(3) Subsurface damage exhibits strong anisotropy. Scratching along the [0001] orientation activates multiple deformation systems, leading to denser but shallower defects, whereas along the $[1\bar{1}00]$ orientation, Prism slip dominates, resulting in deeper damage layers.
(4) By combining an ultrasonic vibration-induced stress model with a Schmid-type criterion, a damage-evolution model for UVAS is established.
(5) The proposed model elucidates the mechanism of damage suppression: by shortening the effective time during which the dominant slip and twinning systems remain above their activation thresholds, it enhances defect inhibition, aligning with the simulation results.

This mechanistic understanding bridges atomic-scale processes with continuum-scale machining responses, enabling rational optimization of the UVAS process for anisotropic sapphire. It is expected to advance the ultra-precision manufacturing of sapphire substrates and to improve the yield and reliability of optoelectronic and power devices.

CRediT authorship contribution statement

Yuqiang Zhang: Writing – original draft, Data curation. **Zhongwei Hu:** Supervision, Funding acquisition, Conceptualization. **Yiqing Yu:** Writing – review & editing, Funding acquisition. **Xipeng Xu:** Writing – review & editing, Methodology. **Wenhan Zeng:** Writing – review & editing, Software. **Wenbin Zhong:** Writing – review & editing, Software. **Qing Peng:** Validation, Resources. **Liam Blunt:** Writing – review & editing, Formal analysis. **Xiangqian Jiang:** Supervision, Project administration.

Declaration of Generative AI and AI-assisted technologies in the writing process

During the preparation of this work the authors used ChatGPT 5.1 in order to refine the language during the final writing stage. After using this tool/service, the authors reviewed and edited the content as needed and took full responsibility for the content of the publication.

Declaration of competing interest

The authors declare that they have no known competing financial interests or personal relationships that could have appeared to influence the work reported in this paper.

Acknowledgments

This research was funded by the National Natural Science Foundation of China (Grant No. 52375429, No. 52175404), and The Future Advanced Metrology Hub for Sustainable Manufacturing (Ref: EP/Z53285X/1).

References

[1] Yue Z, He L, Cui Q, et al. Fabrication of sapphire optical windows with infrared transmittance enhancement and visible transmittance reduction by femtosecond laser direct writing. Opt Laser Technol 2025;188:112989. https://doi.org/10.1016/j.optlastec.2025.112989.
[2] McBride RP, Hoffman BN, Demos SG, et al. Three-dimensional characterization of modifications in sapphire exposed to laser-induced damage using multimodal spectral microimaging. Sci Rep 2025;15(1):31015. https://doi.org/10.1038/s41598-025-16629-7.
[3] Huang Y, Song Y, Liu Y, et al. Direct epitaxy of high-quality a-plane GaN on r-plane sapphire substrate using patterned SiO_2 mask. J Alloys Compd 2025:183071. https://doi.org/10.1016/j.jallcom.2025.183071.
[4] Azmi NS, Mazlan MN, Taib MIM, et al. Impact of nucleation temperature on growth uniformity of GaN on 4-inch dome-patterned sapphire substrate. Mater Sci Semicond Process 2024;173:108177. https://doi.org/10.1016/j.mssp.2024.108177.
[5] Vuong P, Moudakir T, Gujrati R, et al. Scaling up of growth, fabrication, and device transfer process for GaN-based LEDs on H-BN templates to 6-inch sapphire substrates. Adv Mater Technol 2023;8(18):2300600. https://doi.org/10.1002/admt.202300600.
[6] Pingen K, Wolff N, Hinz AM, et al. Growth of non-polar and semi-polar GaN on sapphire substrates by magnetron sputter epitaxy. Appl Surf Sci Adv 2025;26:100722. https://doi.org/10.1016/j.apsadv.2025.100722.
[7] Lee S, Abbas MS, Yoo D, et al. Pulsed-mode metalorganic vapor-phase epitaxy of GaN on graphene-coated c-sapphire for freestanding GaN thin films. Nano Lett 2023;23(24):11578–85. https://doi.org/10.1021/acs.nanolett.3c03333.
[8] Chen H, Lei M, Meng L, et al. Enhanced performance of InGaN light-emitting diodes via high-quality GaN and embedded air voids grown on hexagonal 3D serpentine mask sapphire substrates. ACS Photonics 2023;10(9):3233–41. https://doi.org/10.1021/acsphotonics.3c00646.
[9] Aggarwal V, Ramesh C, Tyagi P, et al. Controlled epitaxial growth of GaN nanostructures on sapphire (11–20) using laser molecular beam epitaxy for photodetector applications. Mater Sci Semicond Process 2021;125:105631. https://doi.org/10.1016/j.mssp.2020.105631.
[10] Chang JC, Tseng EN, Lo YL, et al. HiPIMS-grown AlN buffer for threading dislocation reduction in DC-magnetron sputtered GaN epifilm on sapphire substrate. Vacuum 2023;217:112553. https://doi.org/10.1016/j.vacuum.2023.112553.
[11] Wang S, Zhao Q, Yang X. Surface and subsurface microscopic characteristics in sapphire ultra-precision grinding. Tribol Int 2022;174:107710. https://doi.org/10.1016/j.triboint.2022.107710.
[12] Kwon SB, Min S. Studying mechanism of anisotropic crack generation on C-, R-, A-, and M-planes of sapphire during ultra-precision orthogonal cutting using a visualized slip/fracture activation model. Nanotechnol Precis Eng 2024;7(4). https://doi.org/10.1063/10.0026318.
[13] Wang S, Zhao Q. Subsurface damage in sapphire ultra-precision grinding. J Manuf Process 2024;129:215–37. https://doi.org/10.1016/j.jmapro.2024.08.056.
[14] Zhao B, Wang Y, Peng J, et al. Overcoming challenges: advancements in cutting techniques for high strength-toughness alloys in aero-engines. Int J Extrem Manuf 2024;6(6):062012. https://doi.org/10.1088/2631-7990/ad8117.
[15] Chen T, Xiao H, Feng S, et al. Heterogeneous components removal mechanism and grinding force model from energy aspect in ultrasonic grinding continuous fiber reinforced metal matrix composites. J Mater Process Technol 2024;332:118538. https://doi.org/10.1016/j.jmatprotec.2024.118538.
[16] Biao Z, Hexu YOU, Qing M, et al. Surface integrity characterization of third-generation nickel-based single crystal blade tenons after ultrasonic vibration-assisted grinding. Chin J Aeronaut 2025;38(1):103138. https://doi.org/10.1016/j.cja.2024.07.010.
[17] Xing Y, Xue C, Liu Y, et al. Freeform surfaces manufacturing of optical glass by ultrasonic vibration-assisted slow tool servo turning. J Mater Process Technol 2024;324:118271. https://doi.org/10.1016/j.jmatprotec.2023.118271.
[18] Li S, Liu C, Zhu T, et al. Effects of the thermal treatments on the optical properties of SiO_2 anti-reflective coatings on sapphire windows. Infrared Phys Technol 2024;137:105151. https://doi.org/10.1016/j.infrared.2024.105151.
[19] Bakhtiyari AN, Wu Y, Wang L, et al. Laser machining sapphire via Si-sapphire interface absorption and process optimization using an integrated approach of the Taguchi method with grey relational analysis. J Mater Res Technol 2023;24:663–74. https://doi.org/10.1016/j.jmrt.2023.02.218.
[20] Wang J, Fang F, An H, et al. Laser machining fundamentals: micro, nano, atomic and close-to-atomic scales. Int J Extrem Manuf 2023;5(1):012005. https://doi.org/10.1088/2631-7990/acb134.
[21] Lei J, Shen H, Wu H, et al. Ultrasonic vibration-assisted electrical discharge machining of enclosed microgrooves with laminated electrodes. J Mater Res Technol 2024;30:9521–30. https://doi.org/10.1016/j.jmrt.2024.06.035.
[22] Han Z, Fang X, Miao G, et al. Controllable electrochemical discharge machining with energy–electricity regulation in glycol-based electrolytes. Int J Mech Sci 2023;247:108161. https://doi.org/10.1016/j.ijmecsci.2023.108161.
[23] Zhang Z, Liu J, Hu W, et al. Chemical mechanical polishing for sapphire wafers using a developed slurry. J Manuf Process 2021;62:762–71. https://doi.org/10.1016/j.jmapro.2021.01.004.
[24] Pawar A, Kamble D, Ghorpade RR. Overview on electro-chemical machining of super alloys. Mater Today Proc 2021;46:696–700. https://doi.org/10.1016/j.matpr.2020.12.017.
[25] Zhou M, Zhong M, Xu W. Novel model of material removal rate on ultrasonic-assisted chemical mechanical polishing for sapphire. Friction 2023;11(11):2073–90. https://doi.org/10.1007/s40544-022-0713-7.
[26] Song Y, Shi K, He Z, et al. Wear characteristics evolution of corundum wheel and its influence on performance in creep feed grinding of nickel-based superalloy. Wear 2025;562:205649. https://doi.org/10.1016/j.wear.2024.205649.

[27] Qu S, Yao P, Gong Y, et al. Modelling and grinding characteristics of unidirectional C–SiCs. Ceram Int 2022;48(6):8314–24. https://doi.org/10.1016/j.ceramint.2021.12.036.
[28] Li C, Wang K, Piao Y, et al. Surface micro-morphology model involved in grinding of GaN crystals driven by strain-rate and abrasive coupling effects. Int J Mach Tools Manuf 2024;201:104197. https://doi.org/10.1016/j.ijmachtools.2024.104197.
[29] Liang Z, Wang X, Wu Y, et al. Experimental study on brittle–ductile transition in elliptical ultrasonic assisted grinding (EUAG) of monocrystal sapphire using single diamond abrasive grain. Int J Mach Tools Manuf 2013;71:41–51. https://doi.org/10.1016/j.ijmachtools.2013.04.004.
[30] Zhang C, Feng P, Zhang J. Ultrasonic vibration-assisted scratch-induced characteristics of C-plane sapphire with a spherical indenter. Int J Mach Tools Manuf 2013;64:38–48. https://doi.org/10.1016/j.ijmachtools.2012.07.009.
[31] Xu H, Yin Z, Miao Q, et al. Longitudinal-torsional compound ultrasonic vibration end grinding sapphire: a study on surface topography and roughness. Mater Sci Semicond Process 2024;171:107990. https://doi.org/10.1016/j.mssp.2023.107990.
[32] Zou Y, Hu B, Niu X, et al. Multiscale Mechanistic Insights into Green Anionic Surfactants on Chemical Mechanical Polishing Performance of C-, A-, and R-Plane Sapphire: Combined Experiments and Theoretical Calculations[J]. Langmuir 2025; 41(38):26213–25. https://doi.org/10.1021/acs.langmuir.5c03154.
[33] Verma GC, Pandey PM. Machining forces in ultrasonic vibration assisted end milling. Ultrasonics 2019;94:350–63. https://doi.org/10.1016/j.ultras.2018.07.004.
[34] Wang H, Hu Y, Cong W, et al. A mechanistic model on feeding-directional cutting force in surface grinding of CFRP composites using rotary ultrasonic machining with horizontal ultrasonic vibration. Int J Mech Sci 2019;155:450–60. https://doi.org/10.1016/j.ijmecsci.2019.03.009.
[35] Ni C, Zhu L, Yang Z. Comparative investigation of tool wear mechanism and corresponding machined surface characterization in feed-direction ultrasonic vibration assisted milling of Ti–6Al–4V from dynamic view. Wear 2019;436: 203006. https://doi.org/10.1016/j.wear.2019.203006.
[36] Zhang C, Wang J, Jiao F, et al. Research on tool wear and surface quality in laser-assisted ultrasonic elliptical vibration cutting of cemented carbide. Tribol Int 2024; 193:109389. https://doi.org/10.1016/j.triboint.2024.109389.
[37] Huang W, Hashimoto T, Yan J. Towards understanding the ultrasonic vibration-assisted diamond cutting of ZnO crystals: Surface integrity and tool wear mechanism. J Mater Process Technol 2025:119026. https://doi.org/10.1016/j.jmatprotec.2025.119026.
[38] Lu H, Zhu L, Yang Z, et al. Research on the generation mechanism and interference of surface texture in ultrasonic vibration assisted milling. Int J Mech Sci 2021;208: 106681. https://doi.org/10.1016/j.ijmecsci.2021.106681.
[39] Wang H, Yang G, Su H, et al. Insight into surface formation mechanism during ultrasonic elliptical vibration cutting of tungsten alloy by scratching experiment and molecular dynamics. Tribol Int 2024;191:109088. https://doi.org/10.1016/j.triboint.2023.109088.
[40] Qu S, Sun X, Dong Z, et al. Simulation and experimental investigation of material removal profile based on ultrasonic vibration polishing of K9 optical glass. Tribol Int 2024;196:109730. https://doi.org/10.1016/j.triboint.2024.109730.
[41] Yu H, Liang X, Guo F, et al. Laser-ultrasonic vibration hybrid assisted machining in advanced difficult-to-cut materials: technologies, mechanisms, and challenges. J Mater Process Technol 2025:119076. https://doi.org/10.1016/j.jmatprotec.2025.119076.
[42] Chen Y, Hu Z, Yu Y, et al. Processing and machining mechanism of ultrasonic vibration-assisted grinding on sapphire. Mater Sci Semicond Process 2022;142: 106470. https://doi.org/10.1016/j.mssp.2022.106470.
[43] Huang W, Huang K, Zhong Q, et al. Design of piezoelectric ultrasonic composite vibration system for precision grinding. Micromachines 2025;16(4):408. https://doi.org/10.3390/mi16040408.
[44] Yin Z, Xu H, Miao Q, et al. Research on removal mechanism of longitudinal-torsional compound ultrasonic vibration end grinding sapphire. Surf Interfaces 2025:107690. https://doi.org/10.1016/j.mssp.2023.107990.
[45] Wang Y, Liang Z, Zhao W, et al. Effect of ultrasonic elliptical vibration assistance on the surface layer defect of M-plane sapphire in microcutting. Mater Des 2020; 192:108755. https://doi.org/10.1016/j.matdes.2020.108755.
[46] Ansary SR, Kabir S, Nnokwe C, et al. Ultrasonic vibration-assisted scribing of sapphire: effects of ultrasonic vibration and tool geometry. Int J Adv Manuf Technol 2025;136(7):3559–76. https://doi.org/10.1007/s00170-025-15071-3.
[47] Zhang D, Li H, Tang J, et al. Cutting mechanism and surface characteristics of during ultrasonic vibration-assisted cutting iron alloy: an atomistic investigation. Tribol Int 2026;214:111275. https://doi.org/10.1016/j.triboint.2025.111275.
[48] Liu Z, Tang W, Pan F, et al. Ultrafast phase transformation and strengthening mechanisms in alloys induced by femtosecond laser shock: a novel strategy for intermetallic control. Int J Mach Tools Manuf 2025:104292. https://doi.org/10.1016/j.ijmachtools.2025.104292.
[49] Chen J, Zhu Y, Huang M, et al. Study on the effects of H on the plastic deformation behavior of grain boundaries in nickel by MD simulation. Mater Des 2022;215: 110472. https://doi.org/10.1016/j.matdes.2022.110472.
[50] Lin J, Jiang F, Xu X, et al. Molecular dynamics simulation of nanoindentation on c-plane sapphire. Mech Mater 2021;154:103716. https://doi.org/10.1016/j.mechmat.2020.103716.
[51] Kim WK, Xi D, Kim BH. Nanoscale indentation and scratching tests of single crystal sapphire using molecular dynamics simulation. Comput Mater Sci 2019;170: 109195. https://doi.org/10.1016/j.commatsci.2019.109195.
[52] Liu D, Qi Y, Chen J, et al. Effect of temperature on the mechanical properties and anisotropy of C-plane sapphire: Insights from indentation tests and MD simulations. Vacuum 2025;237:114187. https://doi.org/10.1016/j.vacuum.2025.114187.
[53] Chen J, Qi Y, Liu D, et al. Alternate activation-annihilation of dislocations realizes the plasticity of sapphire during indentation. Mater Des 2024;239:112772. https://doi.org/10.1016/j.matdes.2024.112772.
[54] Xu W, Sheng C, Zhong M. Effects of ultrasonic vibration on sapphire polishing investigated by molecular dynamics. Tribol Int 2022;176:107911. https://doi.org/10.1016/j.triboint.2022.107911.
[55] Xu W, Huang C, Liu X, et al. Influences of ultrasonic vibration directions, amplitudes, and frequencies on sapphire polishing studied by molecular dynamics. Precis Eng 2024;91:155–73. https://doi.org/10.1016/j.precisioneng.2024.09.013.
[56] Zhou M, Cheng Y, Zhong M, et al. Macro and micro-nano machining mechanism for ultrasonic vibration assisted chemical mechanical polishing of sapphire. Appl Surf Sci 2023;640:158343. https://doi.org/10.1016/j.apsusc.2023.158343.
[57] Zhang Y, Hu Z, Yu Y, et al. Crystal-orientation-dependent nanoscale machining mechanisms in ultrasonic vibration-assisted scratching sapphire. Appl Surf Sci 2025:165069. https://doi.org/10.1016/j.apsusc.2025.165069.
[58] Mizumoto Y, Maas P, Kakinuma Y, et al. Investigation of the cutting mechanisms and the anisotropic ductility of monocrystalline sapphire. CIRP Ann 2017;66(1): 89–92. https://doi.org/10.1016/j.cirp.2017.04.018.
[59] He G, Wu H, Huang H, et al. Direct observation of the fracture process on C-plane sapphire by in-situ scratch tests. J Mater Res Technol 2024;31:3825–43. https://doi.org/10.1016/j.jmrt.2024.07.093.
[60] Wang X, Zheng W, Xing H, et al. Influence of crystal orientation on mechanical properties and stress distribution in monocrystalline sapphire. Eng Fract Mech 2025;319:110996. https://doi.org/10.1016/j.engfracmech.2025.110996.
[61] Song C, Xiang D, Yuan Z, et al. Two-dimensional ultrasonic-assisted variable cutting depth scratch force model considering tool wear and experimental verification. Tribol Int 2025;204:110510. https://doi.org/10.1016/j.triboint.2025.110510.
[62] Sun GY, Zhang W, Wang JY, et al. Research on subsurface damage mechanism and suppression method of ultrasonic vibration–assisted grinding of sapphire components under extreme service environment. Int J Adv Manuf Technol 2024; 135(5):2215–42. https://doi.org/10.1007/s00170-024-14491-x.
[63] Lin S, Feng J, Zhang Y, et al. Analytical modelling of both parallel and cross grinding with arc-shaped wheel for grinding-induced damage and grinding force. Int J Adv Manuf Technol 2020;107(1):731–45. https://doi.org/10.1007/s00170-019-04686-y.
[64] Liu H, Zhao P, Wu D, et al. Investigate on material removal of 3C-SiC crystals in nano-polishing via molecular dynamics. J Manuf Process 2024;120:467–77. https://doi.org/10.1016/j.jmapro.2024.04.080.
[65] Qu D, Zhu Z, Zheng M, et al. Multiscale exploration of oxidation kinetics of nickel-based alloys under force-chemical coupling: ReaxFF-MD simulations and nanoindentation experiments. Tribol Int 2025:111465. https://doi.org/10.1016/j.triboint.2025.111465.
[66] Wang H, Kang R, Bao Y, et al. Microstructure evolution mechanism of tungsten induced by ultrasonic elliptical vibration cutting at atomic/nano scale. Int J Mech Sci 2023;253:108397. https://doi.org/10.1016/j.ijmecsci.2023.108397.
[67] Wu Y, Rao Q, Qin Z, et al. A distinctive material removal mechanism in the diamond grinding of (0001)-oriented single crystal gallium nitride and its implications in substrate manufacturing of brittle materials. Int J Mach Tools Manuf 2024;203:104222. https://doi.org/10.1016/j.ijmachtools.2024.104222.
[68] Li C, Yang R, Gao C, et al. Atomic-scale insight into damage and removal behaviors during ultrasonic elliptical vibration-assisted grinding of CaF_2 crystals. J Mater Res Technol 2025;36:1349–61. https://doi.org/10.1016/j.jmrt.2025.03.201.
[69] Qiu T, Jiang F, Wang N, et al. Atomistic understanding of the variable nano-hardness of C-plane sapphire considering the crystal anisotropy. J Mater Res Technol 2024;29:4514–25. https://doi.org/10.1016/j.jmrt.2024.02.161.
[70] Lin J, Jiang F, Wen Q, et al. Deformation anisotropy of nano-scratching on C-plane of sapphire: a molecular dynamics study and experiment. Appl Surf Sci 2021;546: 149091. https://doi.org/10.1016/j.apsusc.2021.149091.
[71] Liu X, Zhong M, Xu W. Molecular dynamics study of sapphire polishing considering chemical products. ECS J Solid State Sci Technol 2023;12(12):124002. https://doi.org/10.1149/2162-8777/ad1617.
[72] Xu Q, Zaborowska A, Mulewska K, et al. Atomistic insights into nanoindentation-induced deformation of α-Al_2O_3 single crystals. Vacuum 2024;219:112733. https://doi.org/10.1016/j.vacuum.2023.112733.
[73] Zhao J, Zhang Q, Chen Y, et al. Damage inhibition mechanisms in ultrasonic vibration-assisted scratching of monocrystalline silicon[J]. Mater Sci Semicond Process 2025;200:109924. https://doi.org/10.1016/j.mssp.2025.109924.
[74] Wu H, Zhang S, Ye X, et al. Unveiling the underlying mechanism of ultrasonic vibration assisted machining: tip-based single asperity nanoscratching experiments and insights from molecular dynamics simulations. J Manuf Process 2025;140: 78–90. https://doi.org/10.1016/j.jmapro.2025.02.047.
[75] Liu H, Guo Y, Li D, et al. Material removal mechanism of FCC single-crystalline materials at nano-scales: chip removal & ploughing. J Mater Process Technol 2021; 294:117106. https://doi.org/10.1016/j.jmatprotec.2021.117106.
[76] Huang Y, Zhou Y, Li J, et al. Materials removal mechanism and multi modes feature for silicon carbide during scratching. Int J Mech Sci 2022;235:107719. https://doi.org/10.1016/j.ijmecsci.2022.107719.
[77] Britton D, Hinojos A, Hummel M, et al. Application of the polyhedral template matching method for characterization of 2D atomic resolution electron microscopy images. Mater Charact 2024;213:114017. https://doi.org/10.1016/j.matchar.2024.114017.

[78] Hu Z, Chen Y, Lai Z, et al. Coupling of double grains enforces the grinding process in vibration-assisted scratch: insights from molecular dynamics. J Mater Process Technol 2022;304:117551. https://doi.org/10.1016/j.jmatprotec.2022.117551.

[79] Tongwei L, Haoxing T, Xin D, et al. Crystallographic dependence of ultrafast laser induced crack generation in single-crystal sapphire[J]. Vacuum 2025;240:114528. https://doi.org/10.1016/j.vacuum.2025.114528.

[80] Fan P, Goel S, Luo X, et al. Origins of ductile plasticity in a polycrystalline gallium arsenide during scratching: MD simulation study. Appl Surf Sci 2021;552:149489. https://doi.org/10.1016/j.apsusc.2021.149489.

[81] Doan DQ, Fang TH. Effect of vibration parameters on the material removal characteristics of high-entropy alloy in scratching. Int J Mech Sci 2022;232: 107597. https://doi.org/10.1016/j.ijmecsci.2022.107597.

[82] Stukowski A. Visualization and analysis of atomistic simulation data with OVITO–the open visualization tool. Model Simul Mater Sci Eng 2009;18(1): 015012. https://doi.org/10.1088/0965-0393/18/1/015012.

[83] Zhang Y, Hu Z, Chen Y, et al. Insights into scratching force in axial ultrasonic vibration-assisted single grain scratching. J Manuf Process 2024;112:150–60. https://doi.org/10.1016/j.jmapro.2024.01.005.

[84] Yalameha S, Nourbakhsh Z, Vashaee D. ElATools: a tool for analyzing anisotropic elastic properties of the 2D and 3D materials. Comput Phys Commun 2022;271: 108195. https://doi.org/10.1016/j.cpc.2021.108195.

[85] Ran Z, Zou C, Wei Z, et al. VELAS: an open-source toolbox for visualization and analysis of elastic anisotropy. Comput Phys Commun 2023;283:108540. https://doi.org/10.1016/j.cpc.2022.108540.

[86] Zhang Y, Hu Z, Yu Y, et al. Anisotropic plastic deformation and damage evolution of sapphire under nanoindentation. Int J Mech Sci 2025:110769. https://doi.org/10.1016/j.ijmecsci.2025.110769.

[87] Wang J, Guo B, Zhao Q, et al. Dependence of material removal on crystal orientation of sapphire under cross scratching. J Eur Ceram Soc 2017;37(6): 2465–72. https://doi.org/10.1016/j.jeurceramsoc.2017.01.032.

[88] Nowak R, Sakai M. The anisotropy of surface deformation of sapphire: Continuous indentation of triangular indenter. Acta Metall Mater 1994;42(8):2879–91. https://doi.org/10.1016/0956-7151(94)90229-1.

[89] Lin W, Shimizu J, Zhou L, et al. Investigation of nanoscratch anisotropy of C-plane sapphire wafer using friction force microscope. Precis Eng 2022;73:51–62. https://doi.org/10.1016/j.precisioneng.2021.08.011.

[90] Maas P, Mizumoto Y, Kakinuma Y, et al. Anisotropic brittle-ductile transition of monocrystalline sapphire during orthogonal cutting and nanoindentation experiments. Nanotechnol Precis Eng 2018;1(3):157–71. https://doi.org/10.1016/j.npe.2018.09.005.

[91] Li C, Piao Y, Zhang F, et al. Understand anisotropy dependence of damage evolution and material removal during nanoscratch of MgF_2 single crystals. Int J Extrem Manuf 2022;5(1):015101. https://doi.org/10.1088/2631-7990/ac9eed.